

Event-based contact angle measurements inside porous media using time-resolved micro-computed tomography

Arjen Mascini¹, Veerle Cnudde^{1,2} & Tom Bultreys¹

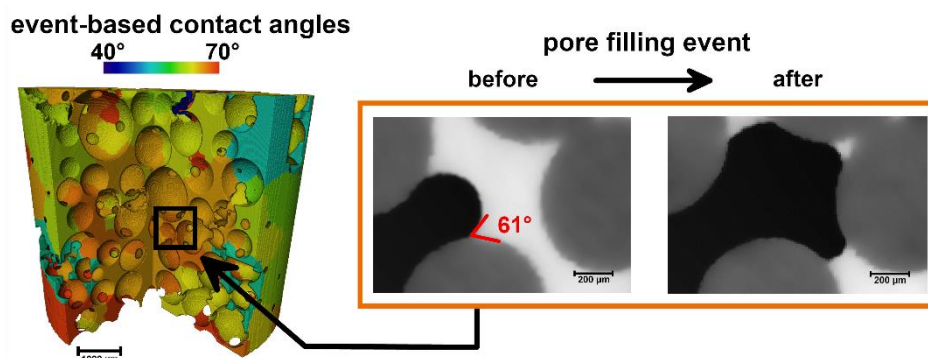
¹ Ghent University, Centre for X-Ray Tomography (UGCT), Pore-scale Processes in Geomaterials Research group (PProGRes), Krijgslaan 281/ S8, 9000 Ghent, Belgium, e-mail: Arjen.Mascini@UGent.be

² Utrecht University, Dept. of Earth Sciences, Environmental hydrogeology, Princetonlaan 8a, 3584 Utrecht, The Netherlands

Abstract

Capillary-dominated multiphase flow in porous materials is strongly affected by the pore walls' wettability. Recent micro-computed tomography (mCT) studies show that contact angles can be measured inside the pores if the fluid distribution is static. However, this may not be directly relevant to dynamic fluid displacements. Here, we approximate receding contact angles locally in time and space on time-resolved mCT datasets of drainage in a glass bead pack and a limestone. Whenever a fluid meniscus suddenly entered one or more pores, geometric and thermodynamically consistent contact angles in the surrounding pores were measured in the time step just prior to the displacement event. We introduce a new force-based contact angle, defined to recover the measured capillary pressure in the invaded pore throat prior to interface movement. While the static method results in unexpectedly wide contact angle distributions, the new geometric and force-based contact angles followed plausible, narrower distributions and were mutually consistent. We were not able to obtain credible results for the thermodynamically consistent event-based method, likely due to uncertainties in image analysis and neglecting viscous dissipation. Time-resolved mCT analysis can yield a more appropriate wettability characterization for pore scale models, despite the need to further reduce image analysis uncertainties.

Graphical abstract



Keywords

Contact angle, Pore-scale, Wettability, Multiphase flow, porous media, imaging, X-ray micro-tomography, interfacial curvature, Haines jump, Primary drainage

33 **1. Introduction**

34 Multiphase flow in porous materials is crucial for e.g. safe subsurface CO₂ storage (Bui
35 et al., 2018), groundwater remediation (Mercer and Cohen, 1990) and efficient PEM
36 fuel cells (Borup et al., 2007; Gostick et al., 2006). This process is strongly affected by
37 the porous medium's wettability: its affinity to be in contact with one fluid over another
38 (Abdallah et al., 2007). The wettability, typically expressed as a contact angle between
39 the solid and the fluids, induces capillary forces which exert a strong influence on fluid
40 displacement (Singh et al., 2019). Drainage is the displacement of a wetting fluid by a
41 non-wetting fluid, while the reverse process is called imbibition (Blunt, 2017).
42 Fundamentally, wettability is a function of the intermolecular forces between the fluids
43 and the solid surface (including any coatings or impurities on it). In addition, most
44 natural materials contain surface roughness from the nanometer scale upwards, which
45 influences the effective contact angle observed at larger scales (Schmatz et al., 2015).
46 Due to local variations in mineralogy, surface roughness and coating, contact angles
47 in porous media are often hysteretic, scale-dependent and variable throughout the
48 pore space (Abdallah et al., 2007; Alhammadi et al., 2017; AlRatrouf et al., 2018;
49 Buckley, 2001; Cassie and Baxter, 1944; Khishvand et al., 2016; Morrow, 1990;
50 Murison et al., 2014; Quéré, 2008; Singh et al., 2016; Wenzel, 1936). One of the main
51 open standing questions is therefore how to define and measure local wettability
52 characteristics throughout the pore space with relevance to multiphase fluid dynamics.
53 This is particularly important to inform pore-scale computational models (Akai et al.,
54 2019b; Verma et al., 2018; Zhao et al., 2019).

55 Recent work has shown that contact angles can be measured by geometrical analysis
56 on a 3D image of fluids in the pore space where the interfaces between the fluids
57 remain static. Such images are typically acquired using micro-computed X-ray
58 tomography (mCT), which has been established as an important tool to investigate
59 multiphase flow at the pore scale in recent years (Andrew et al., 2015; Berg et al.,
60 2013; Blunt, 2017; Bultreys et al., 2016; Wildenschild and Sheppard, 2013). Local
61 measurements of geometrical contact angles in the pore space can be made based
62 on visual observation (Andrew et al., 2015; Khishvand et al., 2017), automated
63 algorithms (AlRatrouf et al., 2017; Scanziani et al., 2017) or methods based on the
64 deficit curvature of the solid and fluid interfaces (Sun et al., 2020). However, these
65 measurements were shown to result in unexpectedly wide distributions of contact
66 angles which are difficult to interpret and to use in pore scale models (Akai et al.,
67 2019a; Blunt et al., 2019). This is not fully explained by the significant uncertainty on
68 determining the three-phase contact line and the normal to the rough solid surface,
69 caused by partial volume effects and other imaging artefacts common in mCT (Cnudde
70 and Boone, 2013).

71 None of the methods discussed so far take into account that contact angles measured
72 on static fluid distributions may not be directly relevant to dynamic fluid displacements
73 during drainage and imbibition. Due to unresolved roughness on the solid surface,
74 contact angles can be hysteretic: at a pinned contact line in any pore, they can vary
75 between an advancing and a receding value, at which the contact line finally starts to
76 move. Furthermore, the location of the contact line in combination with the pore shape
77 at the time of observation, as well as the equilibration time before imaging, likely also

78 influence the observed contact angles (Rabbani et al., 2018; Sun et al., 2020). Such
79 effects cannot be discerned from an image of a fluid distribution at one specific time.
80 Blunt et al. (2019) addressed these concerns by indirectly estimating a
81 thermodynamically consistent contact angle based on energy conservation. They
82 compared mCT images of fluids in a rock sample at the start and end of imbibition, and
83 then equated the pressure-volume work, estimated by measuring the curvature of the
84 fluid-fluid interface and the saturation change, to the interfacial energy stored in the
85 system. The latter can be expressed in function of interfacial areas and a
86 thermodynamically consistent contact angle. The sensitivity to contact line and solid
87 surface normal estimation is therefore reduced or eliminated. Furthermore, this
88 definition aims to take the effects of unresolved solid surface features into account, as
89 it should yield an effective value related to the fluid displacement. Yet, two important
90 issues remain. First, the method assumes that the invasion process can be
91 approximated as being reversible, while this is unlikely to hold for general
92 displacements. (Seth and Morrow, 2007) found that up to 84% of the pressure-volume
93 work during drainage of a limestone was dissipated. Second, the method provides a
94 single contact angle value for the whole sample, rather than a localized measurement.

95 In this work, we propose to estimate pore-scale (receding) contact angles that are
96 relevant to fluid displacement by analyzing time-resolved mCT datasets. First, we
97 identified the time and location of pores in which fluid displacements took place during
98 drainage. Then, geometric and thermodynamically consistent contact angles were
99 computed on a pore-by-pore basis for each single displacement event at the time just
100 before displacement. We introduce a new force-based receding contact angle
101 definition derived from the measured curvature of a fluid meniscus which triggers it to
102 move through a pore throat (i.e. a Haines jump). The method was tested on two publicly
103 available drainage datasets (Schlüter et al., 2016; Singh et al., 2018).

104 The methodology and the experimental data are described in Section 2. In section 3.1,
105 the results from the detection of pore filling events are discussed, followed by a
106 validation of the interfacial curvature analysis by experimental capillary pressure data
107 in Section 3.2. In Section 3.3, the novel time-resolved contact angle measurements
108 are compared to the prior static approach and to each other. This is followed by
109 conclusions and discussion of the current limitations of the method in Section 4.

110 **2. Materials and methods**

111 In the following section, the conceptual framework for this study is first introduced,
112 followed by a brief overview of the experimental data and a detailed description of the
113 image analysis workflow used to identify filling events and calculate force-based,
114 geometric and thermodynamically consistent contact angles.

115 2.1 Contact angles and displacement events

116 At low capillary numbers, drainage takes place as a sequence of spontaneous fluid
117 redistribution events (Haines jumps) every few (tens of) seconds, interspersed by
118 smooth reversible displacement (Armstrong and Berg, 2013; Haines, 1930; Morrow,
119 1970; Schlüter et al., 2017). During the smooth reversible displacement, the contact
120 line can remain (nearly) static close to a local constriction ('pore throat') while the

121 curvature of the interface increases due to the increasing capillary pressure (Figure 1),
122 as described by the Young-Laplace equation:

$$123 \quad P_c = \sigma \left(\frac{1}{R_1} + \frac{1}{R_2} \right) = 2\kappa\sigma \quad (\text{e.q. 1})$$

124 Where σ is the interfacial tension, R_1 and R_2 are the principle radii of curvature of the
125 fluid-fluid interface and κ is its mean curvature.

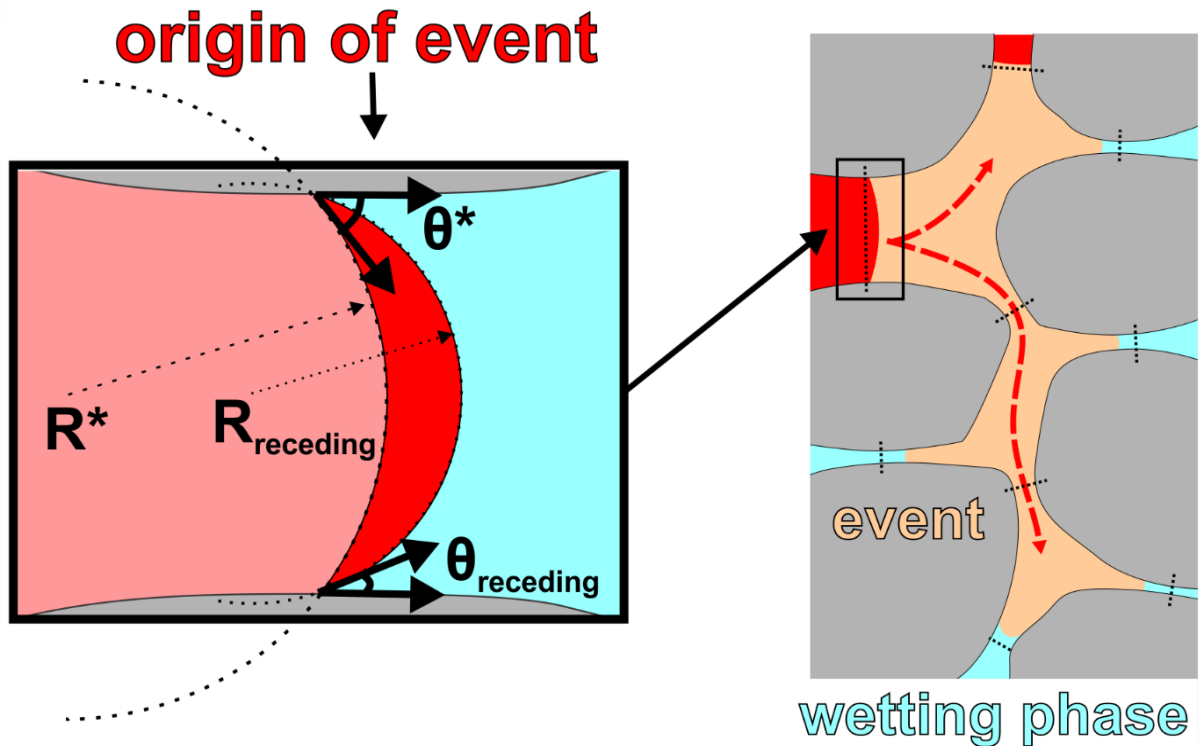
126 When the pressure difference between the two fluids exceeds a certain capillary
127 pressure threshold, an irreversible displacement takes place and the interface abruptly
128 enters one or more neighboring pores (local dilations in the pore space). This threshold
129 is determined by the geometry of the pore throat through which the interface has to
130 pass – the narrower the throat, the higher the threshold – as well as by the local
131 wettability. For example, the associated threshold curvature κ_{thr} in a cylindrical pore
132 throat is given by the well-known Young-Laplace equilibrium pressure:

$$133 \quad P_{c,thr} = 2\sigma\kappa_{thr} = \frac{2\sigma\cos(\theta)}{r} \quad (\text{e.q. 2})$$

134 Where θ is the receding contact angle, and r is the throat radius. Therefore, the local
135 wettability in a pore throat can be characterized by defining a force-based receding
136 contact angle θ_f relevant to the displacement:

$$137 \quad \theta_f \equiv \arccos(\kappa_{thr}r) \quad (\text{e.q. 3})$$

138 Note that the force-based contact angle only yields the same value as the receding
139 contact angle for perfectly cylindrical pore throats. However, the advantage is that it
140 provides a direct link to the threshold capillary pressure without depending on highly
141 scale-dependent measurements at or near the rough solid interface. Furthermore, e.q.
142 3 can in principle be extended to arbitrarily complex geometrical pore throat models,
143 e.g. pore throats with triangular (Ma et al., 1996) or hyperbolic polygonal cross-sections
144 (Joekar-Niasar et al., 2010). In this paper, we used the cylindrical model to obtain a
145 first order estimate of the force-based receding contact angle for several hundreds of
146 Haines jumps in a bead pack and a limestone. The following sections describe how θ_f
147 can be estimated for each individual displacement event in time-resolved mCT
148 datasets, as well as how geometrical and thermodynamically consistent contact angles
149 were determined for comparison.



150

151 *Figure 1 A schematic drawing of a Haines jump during primary drainage. **Left box:** at time $T-1$ the main*
 152 *terminal meniscus of the non-wetting phase (in pink) is located in a pore throat with an interface with a*
 153 *certain radius of curvature (R^*) and associated contact angle θ^* . Just before displacement (in red), the*
 154 *interface reaches a radius of curvature (R_{receding}) and an associated contact angle θ_{receding} upon which it*
 155 *will start to move into the next pore. R_{receding} determines the threshold capillary pressure for the event.*
 156 ***Right box:** in the resulting displacement event, three neighboring pores (indicated in orange and*
 157 *separated by constrictions indicated as black dotted lines) are filled by the Haines jump. Fluid*
 158 *distributions at $T-1$ are in red and at time T in orange.*

159 2.2 Experimental data

160 Two well-documented and publicly available primary drainage data sets were
 161 analyzed: one measured on a sintered glass bead pack (Schlüter et al., 2016) and one
 162 on a Ketton limestone (Singh et al., 2018). Both experiments are unsteady-state
 163 drainage experiments in which a non-wetting phase is injected into a cylindrical sample
 164 at a low capillary number to ensure capillary dominated flow. A summary of the
 165 experimental parameters is given in Table 1. The time resolved mCT experiments
 166 resulted in a series of segmented 3D images, each representing the fluid distribution
 167 in the pore space during a discrete, short time interval in the drainage. The data used
 168 in our analysis, is the segmented data by Schlüter et al., (2016) and (Singh et al.,
 169 2018). The former used a modified form of Markov random field (MRF) segmentation
 170 for this, the latter a seeded watershed algorithm.

171

172

173

174

175 *Table 1 Overview of the data sets used for the image analysis. * exact flow rates were not recorded*
 176 *during the drainage experiments.*

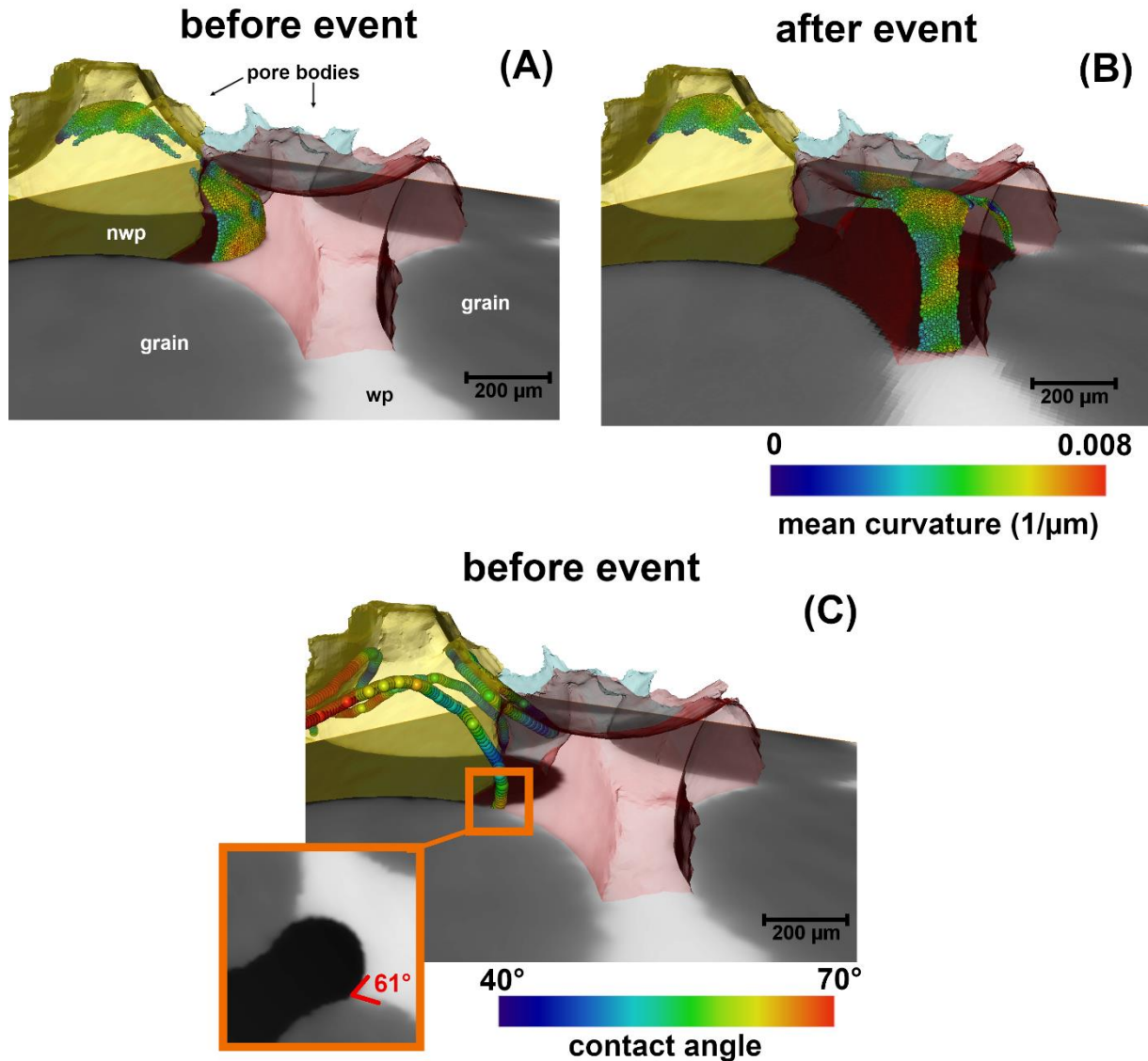
	glass bead pack	Ketton limestone
Sample dimension	5.8mm dia. x 7mm long	3.8mm dia. x 10mm long
Boundary condition	constant flowrate	constant pressure + tight capillary plate
Fluids	n-dodecane, CsCl-brine	n-decane, KI-brine
Interfacial tension	36mN/m	52.33mN/m
Flow rate	50 μ l/h	\sim 1-6 μ l/h*
Imposed pressure	N/A	50kPa
Capillary number	$4.2 \cdot 10^{-8}$	$\sim 10^{-9}$ *
Number of time steps	38	496
Time per time step	113s	38s
Time span (hr:min:sec)	01:13:44	5:14:08
Reconstructed voxel size	8.4 μ m	3.28 μ m
Reference	Schlüter et al., (2016)	Singh et al., (2018)

177

178 2.3 Image analysis

179 2.3.1 Identifying fluid filling events in time-resolved mCT datasets

180 As a first step in the analysis, the pore space was divided into individual pores
 181 separated by throat surfaces using a watershed algorithm implemented in the open
 182 source algorithm “pnextract” (Raeini et al., 2018) (Figure 2). This algorithm determines
 183 the largest inscribed spheres in each pore and in each throat. Pore and throat radii
 184 were found as the radii of these inscribed spheres. Following the procedure proposed
 185 in Bultreys et al. (2018), 3D images of the determined inscribed spheres in the pores
 186 were overlain on the drainage datasets. The fluid occupancy of pore centers was then
 187 determined by checking if the majority of the voxels in the associated inscribed sphere
 188 were filled with wetting or non-wetting phase. This was done for each pore in each time
 189 step, and “fluid filling” was consecutively found as the case where a pore changes its
 190 fluid occupancy (i.e. the fluid in the majority of its inscribed sphere’s voxels) in
 191 consecutive time steps. Connected fluid fillings in the same time step were regarded
 192 to belong to the same filling event (Figure 1). This was done by performing a graph-
 193 based connectivity clustering of the pores filled in each time step using MATLAB
 194 (Bultreys et al., 2015). Finally, the result of this analysis was a list of filling events,
 195 detailing the time of filling, the pores that were filled (including location and
 196 characterization of the pores), and the pores and throats that neighbor each filling
 197 event. The source throat of each event was found by selecting the throat neighbor with
 198 the largest throat radius.



199

200 *Figure 2 Capturing and characterizing a pore filling event in the sintered glass bead pack dataset from*
 201 *Schlüter et al. (2016). nwp = non-wetting phase, wp = wetting phase. (A) before the event, a non-wetting*
 202 *phase terminal meniscus is located at a pore throat of the yellow pore body. The interface has a mean*
 203 *curvature proportional to the local capillary pressure. (B) at the time step after the event, the interface*
 204 *has moved into the neighboring blue and red pore bodies. (C) the event-based geometric contact angle*
 205 *(62°) is calculated by measuring the contact angle on the points of three-phase contact line, indicated*
 206 *by colored spheres. A manual measurement (small box) of the contact angle in the plane perpendicular*
 207 *to the grain surface is in reasonable agreement (61°) with the event-based geometric contact angle.*

208 2.3.2 Force-based receding contact angles

209 As defined in section 2.1, an estimate for the force-based contact angle can be
 210 obtained by linking the local capillary pressure which triggered the fluid redistribution
 211 to the radius of the source throat of each event. On 3D images of fluid distributions,
 212 the local capillary pressure can be estimated from the curvature of the fluid–fluid
 213 interface (Andrew et al., 2014a; Armstrong et al., 2012). As the volume in space
 214 associated to each pore is known, it is straightforward to map point measurements of
 215 interfacial curvature to pores. At time step T-1, before a filling event, the fluid–fluid
 216 interface is located (partly) in the pores directly neighboring the event. Therefore, we

217 determined the average fluid-fluid interfacial curvature both in pores that were invaded
218 and in their neighbors during the time-step just before the associated filling event
219 (Figure 2A).

220 To obtain curvature values, the fluid-fluid interface was extracted from the segmented
221 images by extracting a triangulated surface using the marching cube algorithm
222 (Lorensen and Cline, 1987) in Avizo (ThermoFisher Scientific). Constrained surface
223 smoothing using a Gaussian filter with an extent of 3 voxels was performed, analogous
224 to Li et al. (2018). Mean surface curvature was calculated using the eigenvalues and
225 eigenvectors of a quadratic form fitted locally to the surface. The accuracy of this
226 calculation is limited by the finite resolution of the images, especially in regions close
227 to the three-phase contact line, where partial volume effects add to the uncertainty,
228 and in arc-meniscus sections of the fluid-fluid interface (Akai et al., 2019b; Armstrong
229 et al., 2012; Li et al., 2018; Singh et al., 2017). The curvature data points were filtered
230 based on several criteria to account for this. First, all data points with a curvature
231 corresponding to a radius of curvature smaller than twice the reconstructed voxel size
232 were omitted as these most likely represent noise. The non-wetting phase bulges into
233 the wetting phase during drainage and terminal menisci thus have a positive curvature
234 with respect to the non-wetting phase (Armstrong et al., 2012). As this study is limited
235 to drainage, all data points with a curvature equal to or smaller than zero, typically
236 associated with arc-meniscus sections of the interface, were subsequently filtered out.
237 Lastly, we followed the approach of Li et al. (2018) on the glass bead data set, to filter
238 and weigh the curvature data points based (AlRatrou et al., 2017; Blunt et al., 2019;
239 Dalton et al., 2018) on their geodesic distance (20% of the maximum geodesic distance
240 found in the image) to the edge of the surface. For the Ketton data set, we followed the
241 approach of Singh et al. (2017) by filtering data points with a Euclidian distance of 3
242 voxels from the pore wall.

243 2.3.3 Geometric (receding) contact angles

244 To reduce uncertainty related to the state of the interface (e.g. pinning), receding
245 contact angles have to be measured at (or at least very near) the moment the fluid-
246 fluid interface moves. Therefore, we propose to measure geometric contact angles at
247 the appropriate time step in a small region directly surrounding the displacement event
248 in time-resolved mCT data. This is in contrast to previous measurements of geometric
249 contact angles that included all points on the three phase contact lines in a single mCT
250 image of a static fluid distribution, typically acquired at the end of drainage or imbibition
251 (e.g. AlRatrou et al., 2017; Blunt et al., 2019; Dalton et al., 2018).

252 We compared both approaches of contact angle measurements using the fully
253 automatic algorithm developed by AlRatrou et al. (2017). The algorithm generated a
254 smoothed mesh on which the three phase contact line is identified. Subsequently, it
255 calculated geometric contact angles in each mesh point on the contact line based on
256 the dot product of the vectors normal to the solid surface and the fluid-fluid interface.
257 We used the default smoothing settings proposed by AlRatrou et al. (2017). The
258 method was applied to each time step image. Event-based geometric contact angles
259 were then determined by retaining and averaging only the geometric contact angle
260 points measured in the event pores and their neighbors at the appropriate event time

261 step (Figure 2C). We compared this to the conventional static method by calculating
 262 the distribution of all the contact angle points in the last time step of drainage.

263 2.3.4 Thermodynamically-consistent receding contact angles

264 Here, we extend the work of Morrow (1970) and Blunt et al. (2019) to derive a
 265 thermodynamically-consistent contact angle, θ_t , for filling events during primary
 266 drainage:

$$267 \quad \cos\theta_t = \frac{\kappa_{thr}\Delta V_{nwp} + \Delta A_{fluid-fluid}}{\Delta A_{nwp-solid}} \quad (\text{e.q. 4})$$

268 Where κ_{thr} is the threshold curvature at invasion, ΔV_{nwp} the change in volume of the
 269 non-wetting phase (positive for primary drainage), $\Delta A_{fluid-fluid}$ the change in fluid-fluid
 270 interfacial area, and $\Delta A_{nwp-solid}$ the change in non-wetting-solid surface area (positive
 271 for primary drainage). Surface areas were calculated on triangulated surfaces
 272 extracted using the method described in Section 2.3.2. By applying this relationship,
 273 drainage is assumed to be an isothermal, reversible process, which has been shown
 274 not to be valid in general (Armstrong and Berg, 2013; Morrow, 1970; Seth and Morrow,
 275 2007). The calculated thermodynamically-consistent contact angle is therefore likely
 276 an underestimation, as part of the work done will be lost as viscous dissipation (Blunt
 277 et al., 2019). Similar to the calculation of the geometric receding contact angle, we
 278 compare the event-by-event based results to a static calculation using surface areas,
 279 curvatures and volumes of consecutive time step images.

280 **3. Results & discussion**

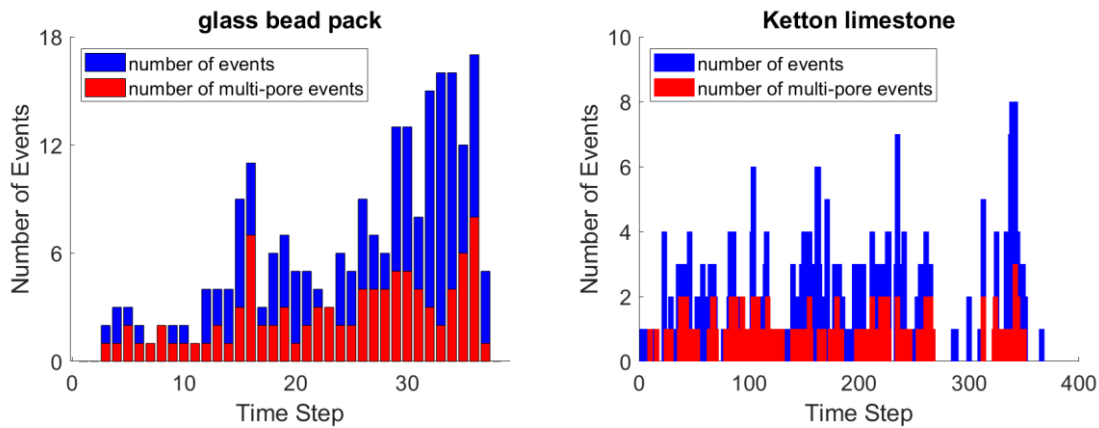
281 3.1 Filling events

282 By detecting changes in pore occupancy during the experiments and clustering these
 283 into pore filling events (section 2), 231 (glass bead pack) and 425 (Ketton limestone)
 284 filling events were detected and analyzed. Up to 17 (glass beads) and 8 (Ketton
 285 limestone) different events were detected in a single time step (Figure 3). The number
 286 of pore-filling events per time step increases over time (Figure 3) while the volumes of
 287 these events decreases (Figure 4). Well connected, larger pores were filled first, and
 288 smaller pores with fewer connections were filled later in the sequence, as expected
 289 from invasion percolation.

290 *Table 2 Overview of the detected events in the glass bead pack and Ketton limestone*

	glass bead pack	Ketton limestone
Events	231	425
multi-pore events	95	134
Large events (>1% pore volume, #pores)	20	4
Largest event (# pores)	18	46

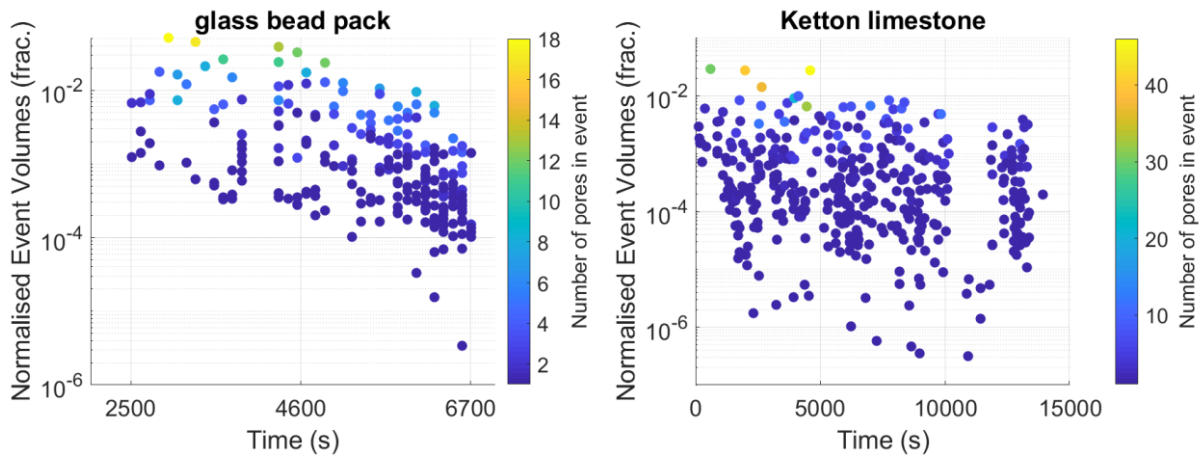
291



292

293 *Figure 3 Bar charts showing the number of (multi-pore) events detected per time step.*

294

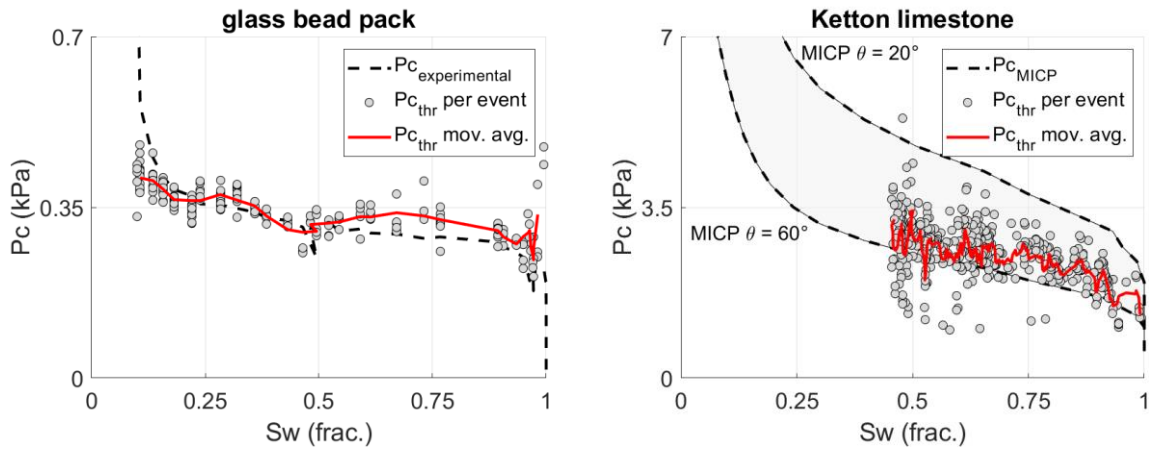


295

296 *Figure 4 Plots showing the normalized event volume for each event with the number of pores filled*
 297 *during the event in colors.*

298 3.2 Validation of curvature measurements

299 The force-based contact angle introduced in this paper depends crucially on the
 300 measurement of interfacial curvature from the time-resolved mCT scans. Using e.q. 1,
 301 these measurements also yield the associated capillary pressure, which can be plotted
 302 against the wetting saturation determined from the image (Figure 5). The resulting
 303 threshold capillary pressures can thus be compared and validated to capillary pressure
 304 curves measured with external pressure transducers (Armstrong et al., 2012).
 305 Experimental pressure measurements were available for the glass bead pack dataset,
 306 but not for the Ketton limestone dataset. We validated the latter using mercury intrusion
 307 capillary pressure (MICP) data, measured on a different Ketton limestone sample
 308 (Reynolds and Krevor, 2015). We rescaled the saturation axis of the MICP data to
 309 include only the pore space larger than the voxel size of the images ($3.28\mu\text{m}$). The P_c
 310 axis was rescaled using the interfacial tension measured by (Singh et al., 2018) and a
 311 range of contact angle values (20° - 60°) expected for Ketton limestone.



312

313 *Figure 5 Calculated threshold capillary pressure for each event plotted against the wetting-phase*
 314 *saturation of the sample calculated from the images. The data is compared to experimental pressure*
 315 *measurements in the case of the glass bead pack and scaled MICP measurements (Reynolds and*
 316 *Krevor 2015) using a theta between 20° and 60° for the data of the Ketton limestone.*

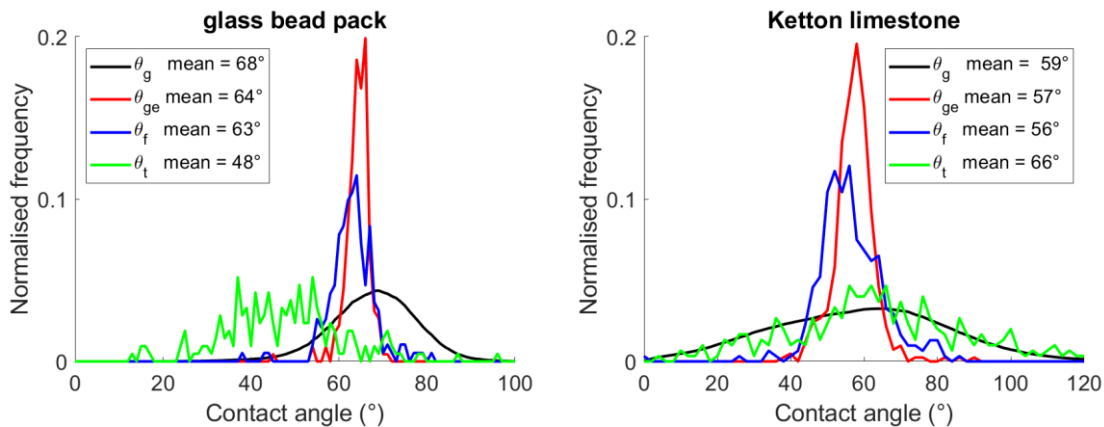
317 As can be seen in Figure 5, the event-based calculations scatter around the externally
 318 measured pressures. The scatter is to some extent expected for drainage, since non-
 319 local effects can induce local pressure differences and the time scale of the
 320 experiments is likely too short to establish full capillary equilibrium (Armstrong and
 321 Berg, 2013; Schlüter et al., 2017).

322 Imaging and image analysis form additional sources of uncertainty. Limited spatial
 323 resolution causes uncertainty in the calculated mean curvature of the interface as the
 324 curvature is not fully resolved. Akai et al. (2019) estimated that local capillary pressures
 325 can be estimated within 30% if the average radius of curvature is more than 6 times
 326 the image resolution. Applying these rules of thumb, a radius of curvature of 6 times
 327 the image resolution would be equivalent to capillary pressures of ~0.7 kPa and ~2.6
 328 kPa for the glass beads and Ketton limestone respectively. As these values are close
 329 to the measured pressures, the spatial resolution is likely to influence the results,
 330 especially at lower wetting phase saturations. The limited temporal resolution of the
 331 scans causes motion artefacts and decreases the signal to noise ratio, providing
 332 additional sources of uncertainty. Furthermore, this also means that the curvature is
 333 determined a few tens of seconds before the Haines jump. To estimate the uncertainty
 334 induced by this, we determined the average rate of change of the external Pc
 335 measurement in the glass bead pack. This was ~43 Pa per time step, equating to an
 336 uncertainty of approximately 10% on the average measured event pressures.
 337 However, the uncertainty is less significant in the beginning of drainage, and more
 338 significant at the very end (when the Pc is changing more rapidly). The temporal
 339 uncertainty on the Ketton dataset can be assumed to be lower, as both the flow rate
 340 and the time per image are smaller (Table 1), yet there are no external pressure
 341 measurements available to estimate this quantitatively. Newer synchrotron beamline
 342 setups allow to further increase the temporal resolution by 2 orders of magnitude
 343 (1s/scan) without compromising the image quality (Mokso et al., 2017; Spurin et al.,
 344 2019).

345

3.3 Force-based, geometric and thermodynamically consistent contact angles

The distribution of the force-based contact angles is compared to those of the static and event-based geometric contact angles and of the event-based thermodynamically consistent contact angles in Figure 6. The average force-based contact angle was 63° and 56° in respectively the glass bead pack and the Ketton limestone datasets, compared to an average event-based geometric contact angle of respectively 64° and 57° . The distribution of the event-based geometric contact angles matched the force-based angle closely. The event-based geometric contact angle has a notably narrower distribution than its “static” counterpart (the distribution of all geometric contact angles measured in one time step image). This confirms that the unexpectedly wide contact angle distributions reported in literature are to a significant extent related to the dynamics of the interface motion, e.g. contact angle hysteresis, pinning, the location of the contact line at the time of fluid redistribution, or interface relaxation. The event-based thermodynamically consistent contact angles are more broadly distributed than the geometric and force-based methods. They had a lower mean value than the other methods for the glass beads (48°) and a higher value for Ketton limestone (66°). Similar values, 44° and 68° for the glass bead pack and Ketton limestone respectively, were found when using the approach of Blunt et al. (2019), using the full fluid distributions on consecutive images for the calculations.



365

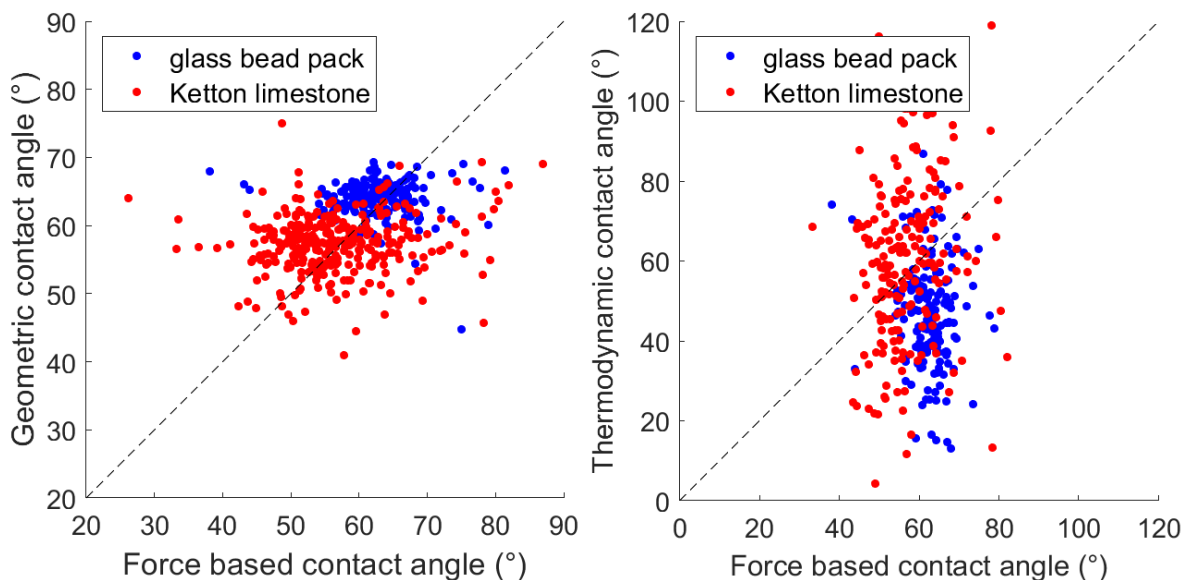
366 *Figure 6 Distribution of force-based (θ_f), geometric (θ_{ge}) and thermodynamically consistent (θ_t) contact*
 367 *angles determined on an event-by-event basis using the proposed methodology, compared to the*
 368 *standard approach of determining the geometric contact angles in each point on the contact line of the*
 369 *mCT image taken after drainage (θ_g).*

370 The contact angle values for each event are cross-plotted in Figure 7. The fairly good
 371 match between the force-based and the geometric methods suggests that geometric
 372 contact angles can be used to provide a reasonable prediction of the invasion capillary
 373 pressure in pore scale drainage models, yet only when measured on an event-by-event
 374 basis in a time-resolved dataset. This is crucial for e.g. pore network modelling studies,
 375 which predict the drainage filling sequence by sequentially invading pores in order of
 376 increasing threshold capillary pressure (invasion percolation). However, it is also clear
 377 that there was still a significant amount of scatter in the data, related to the spatial and
 378 temporal resolutions on the one hand and the irregular shape of the throats in realistic
 379 porous materials on the other hand. The latter could be improved by refining the
 380 definition of the force-based contact angle (e.q. 2). Both sources of uncertainty are

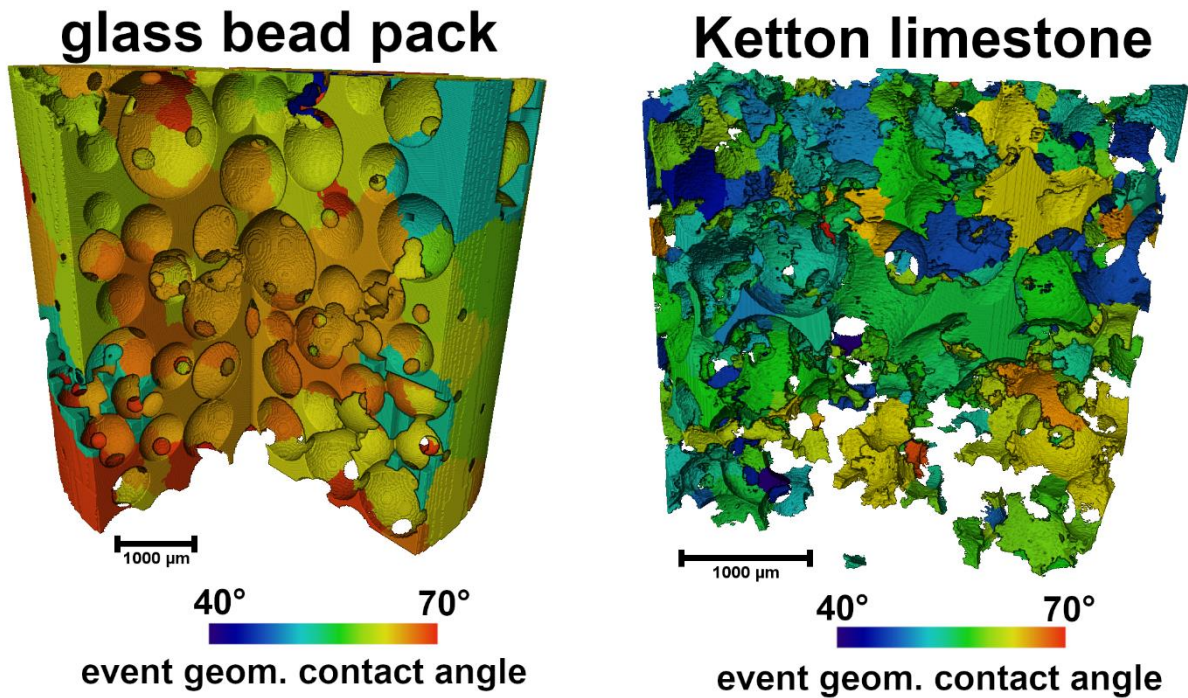
381 consistent with higher scatter in Ketton than in the simpler, wider pore space of the
 382 glass bead pack. The calculated thermodynamically consistent contact angles show
 383 significantly more scattering than the force-based contact angles (Figure 7). In
 384 addition, the equation yielded imaginary values for the contact angle for 17 events in
 385 the glass bead pack data set and 125 in the Ketton limestone data set. The increased
 386 scatter could be attributed to both the added uncertainty in the calculations of fluid-fluid
 387 and fluid-solid surface areas and the assumption of no viscous dissipation.

388 Intuitively, receding contact angles in smooth, water-wet media are expected to be
 389 lower than the reported values. Manual observations using the method described by
 390 Andrew et al. (2014b) confirmed contact angles around 50° - 60° (e.g. Figure 2) in both
 391 the glass beads and Ketton limestone data set, showing that these were likely not
 392 induced by the automatic image analysis method. As shown in Figure 7, the calculated
 393 values were consistent with a description of the fluid displacement at the scale of
 394 observation, and can thus be used directly for pore scale modelling. The discrepancy
 395 may be due to the converging geometry of pore throats, which was shown to increase
 396 the “effective” contact angle (i.e. the one linked to the fluid-fluid interfacial curvature)
 397 (Rabbani et al., 2018). Finally, it should also be noted that the limited temporal
 398 resolution of the mCT data tended to yield an underestimation of the fluid-fluid
 399 curvature, as the capillary pressure rises continuously during image acquisition,
 400 resulting in a slight overestimation of the contact angles.

401 As shown in Figure 8, the values of event-based contact angles can be mapped back
 402 to the original pore space. This spatial data could be used to improve numerical
 403 simulations of multiphase flow by incorporating local information on the wettability of
 404 the sample, which could be especially valuable for samples with a mixed-wettability.



405
 406 *Figure 7 Left: the geometric versus the force-based contact angle for individual events detected in the*
 407 *two drainage datasets. Right: the thermodynamically consistent versus the force-based contact angle*
 408 *for individual events in the two drainage datasets.*



409

410 *Figure 8 Rendering of the 3D distribution of the event-based geometric contact angle for each pore.*

411 **4. Conclusion and outlook**

412 This work aims to improve our understanding of wettability by calculating receding
413 contact angles for individual pore-filling events, rather than for a static fluid distribution
414 as a whole. The proposed method was applied to two unsteady state drainage data
415 sets: a sintered glass bead pack and a Ketton limestone. Event-based geometric
416 contact angles show a distinctively narrower distribution than when these are
417 calculated on the entire static fluid distributions (e.g. AlRatrouf et al., 2017; Blunt et al.,
418 2019; Dalton et al., 2018), suggesting that wide contact angle distributions are likely
419 caused by the unaccounted for dynamics of the interface. We introduce a force-based
420 contact angle, which shows that event-based geometric contact angles produce
421 plausible threshold capillary pressures for associated pore filling events. This suggest
422 that event-based geometric contact angles may provide valid effective contact angles
423 for the displacement process and are more appropriate for use in pore scale modeling.
424 Despite these promising first results, we note the need for enhanced image quality and
425 image processing methodologies to reduce the uncertainty of the proposed methods.
426 Due to these uncertainties, we were not able to draw conclusions on the
427 appropriateness of the thermodynamic contact angle as a concept.

428 Future work should point out if the described method can be used to quantify wettability
429 for mixed-wettability systems and during imbibition. The success hereof would benefit
430 of the increased temporal and spatial resolution available at synchrotron facilities
431 optimized for fast imaging (Mokso et al., 2017) and advances in iterative reconstruction
432 techniques developed for low signal to noise ratios (Chen et al., 2008; Myers et al.,
433 2011). This enhanced image quality is crucial to distinguish different displacement
434 mechanism during imbibition and to improve the accuracy in calculating interfacial
435 curvature and area.

436 **Acknowledgements**

437 Dr. Steffen Schlüter and Dr. Kamaljit Singh are thanked for making their data available
438 and their helpful discussions. This research received funding from the Research
439 Foundation–Flanders (FWO, project G051418N). Tom Bultreys is a postdoctoral fellow
440 of the Research Foundation–Flanders (FWO) and acknowledges its support under
441 grant 12X0919N. The data used in this manuscript is freely available online, as cited
442 in the main text.

443

444 **References**

- 445 Abdallah, W., Buckley, J.S., Carnegie, A., Edwards, J., Herold, B., Fordham, E., Graue, A., Habashy, T.,
446 Seleznev, N., Signer, C., Hussain, H., Montaron, B., Ziauddin, M., 2007. Fundamentals of
447 Wettability. *Oilfield Review* 18.
- 448 Akai, T., Alhammadi, A.M., Blunt, M.J., Bijeljic, B., 2019a. Modeling Oil Recovery in Mixed-Wet Rocks:
449 Pore-Scale Comparison Between Experiment and Simulation. *Transport in Porous Media* 127,
450 393–414. <https://doi.org/10.1007/s11242-018-1198-8>
- 451 Akai, T., Lin, Q., Alhosani, A., Bijeljic, B., Blunt, M., 2019b. Quantification of Uncertainty and Best
452 Practice in Computing Interfacial Curvature from Complex Pore Space Images. *Materials* 12,
453 2138. <https://doi.org/10.3390/ma12132138>
- 454 Alhammadi, A.M., AlRatrou, A., Singh, K., Bijeljic, B., Blunt, M.J., 2017. In situ characterization of
455 mixed-wettability in a reservoir rock at subsurface conditions. *Scientific Reports* 7.
456 <https://doi.org/10.1038/s41598-017-10992-w>
- 457 AlRatrou, A., Blunt, M.J., Bijeljic, B., 2018. Wettability in complex porous materials, the mixed-wet
458 state, and its relationship to surface roughness. *Proceedings of the National Academy of
459 Sciences* 201803734. <https://doi.org/10.1073/pnas.1803734115>
- 460 AlRatrou, A., Raeini, A.Q., Bijeljic, B., Blunt, M.J., 2017. Automatic measurement of contact angle in
461 pore-space images. *Advances in Water Resources* 109, 158–169.
462 <https://doi.org/10.1016/j.advwatres.2017.07.018>
- 463 Andrew, M., Bijeljic, B., Blunt, M.J., 2014a. Pore-by-pore capillary pressure measurements using X-ray
464 microtomography at reservoir conditions: Curvature, snap-off, and remobilization of residual
465 CO₂. *Water Resources Research* 50, 8760–8774. <https://doi.org/10.1002/2014WR015970>
- 466 Andrew, M., Bijeljic, B., Blunt, M.J., 2014b. Pore-scale contact angle measurements at reservoir
467 conditions using X-ray microtomography. *Advances in Water Resources* 68, 24–31.
468 <https://doi.org/10.1016/j.advwatres.2014.02.014>
- 469 Andrew, M., Menke, H., Blunt, M.J., Bijeljic, B., 2015. The Imaging of Dynamic Multiphase Fluid Flow
470 Using Synchrotron-Based X-ray Microtomography at Reservoir Conditions. *Transport in
471 Porous Media* 110, 1–24. <https://doi.org/10.1007/s11242-015-0553-2>
- 472 Armstrong, R.T., Berg, S., 2013. Interfacial velocities and capillary pressure gradients during Haines
473 jumps. *Physical Review E* 88, 043010.
- 474 Armstrong, R.T., Porter, M.L., Wildenschild, D., 2012. Linking pore-scale interfacial curvature to
475 column-scale capillary pressure. *Advances in Water Resources* 46, 55–62.
476 <https://doi.org/10.1016/j.advwatres.2012.05.009>
- 477 Berg, S., Ott, H., Klapp, S.A., Schwing, A., Neiteler, R., Brussee, N., Makurat, A., Leu, L., Enzmann, F.,
478 Schwarz, J.-O., Kersten, M., Irvine, S., Stampanoni, M., 2013. Real-time 3D imaging of Haines
479 jumps in porous media flow. *Proceedings of the National Academy of Sciences* 110, 3755–
480 3759. <https://doi.org/10.1073/pnas.1221373110>
- 481 Blunt, M.J., 2017. *Multiphase Flow in Permeable Media: A Pore-Scale Perspective*. Cambridge
482 University Press.
- 483 Blunt, M.J., Lin, Q., Akai, T., Bijeljic, B., 2019. A thermodynamically consistent characterization of
484 wettability in porous media using high-resolution imaging. *Journal of Colloid and Interface
485 Science* 552, 59–65. <https://doi.org/10.1016/j.jcis.2019.05.026>
- 486 Borup, R., Meyers, J., Pivovar, B., Kim, Y.S., Mukundan, R., Garland, N., Myers, D., Wilson, M., Garzon,
487 F., Wood, D., Zelenay, P., More, K., Stroh, K., Zawodzinski, T., Boncella, J., McGrath, J.E.,
488 Inaba, M., Miyatake, K., Hori, M., Ota, K., Ogumi, Z., Miyata, S., Nishikata, A., Siroma, Z.,
489 Uchimoto, Y., Yasuda, K., Kimijima, K., Iwashita, N., 2007. Scientific Aspects of Polymer
490 Electrolyte Fuel Cell Durability and Degradation. *Chemical Reviews* 107, 3904–3951.
491 <https://doi.org/10.1021/cr050182l>
- 492 Buckley, J.S., 2001. Effective wettability of minerals exposed to crude oil. *Current Opinion in Colloid &
493 Interface Science* 6, 191–196. [https://doi.org/10.1016/S1359-0294\(01\)00083-8](https://doi.org/10.1016/S1359-0294(01)00083-8)

- 494 Bui, M., Adjiman, C.S., Bardow, A., Anthony, E.J., Boston, A., Brown, S., Fennell, P.S., Fuss, S., Galindo,
495 A., Hackett, L.A., Hallett, J.P., Herzog, H.J., Jackson, G., Kemper, J., Krevor, S., Maitland, G.C.,
496 Matuszewski, M., Metcalfe, I.S., Petit, C., Puxty, G., Reimer, J., Reiner, D.M., Rubin, E.S., Scott,
497 S.A., Shah, N., Smit, B., Trusler, J.P.M., Webley, P., Wilcox, J., Mac Dowell, N., 2018. Carbon
498 capture and storage (CCS): the way forward. *Energy & Environmental Science* 11, 1062–1176.
499 <https://doi.org/10.1039/C7EE02342A>
- 500 Bultreys, T., Boone, M.A., Boone, M.N., De Schryver, T., Masschaele, B., Van Loo, D., Van Hoorebeke,
501 L., Cnudde, V., 2015. Real-time visualization of Haines jumps in sandstone with laboratory-
502 based microcomputed tomography. *Water Resources Research* 51, 8668–8676.
503 <https://doi.org/10.1002/2015WR017502>
- 504 Bultreys, T., De Boever, W., Cnudde, V., 2016. Imaging and image-based fluid transport modeling at
505 the pore scale in geological materials: A practical introduction to the current state-of-the-art.
506 *Earth-Science Reviews* 155, 93–128. <https://doi.org/10.1016/j.earscirev.2016.02.001>
- 507 Bultreys, T., Lin, Q., Gao, Y., Raeini, A.Q., AlRatrou, A., Bijeljic, B., Blunt, M.J., 2018. Validation of
508 model predictions of pore-scale fluid distributions during two-phase flow. *Physical Review E*
509 97. <https://doi.org/10.1103/PhysRevE.97.053104>
- 510 Cassie, A.B.D., Baxter, S., 1944. Wettability of porous surfaces. *Transactions of the Faraday Society*
511 40, 546. <https://doi.org/10.1039/tf9444000546>
- 512 Chen, G.-H., Tang, J., Leng, S., 2008. Prior image constrained compressed sensing (PICCS): a method
513 to accurately reconstruct dynamic CT images from highly undersampled projection data sets.
514 *Medical physics* 35, 660–663.
- 515 Cnudde, V., Boone, M.N., 2013. High-resolution X-ray computed tomography in geosciences: A
516 review of the current technology and applications. *Earth-Science Reviews* 123, 1–17.
517 <https://doi.org/10.1016/j.earscirev.2013.04.003>
- 518 Dalton, L.E., Klise, K.A., Fuchs, S., Crandall, D., Goodman, A., 2018. Methods to measure contact
519 angles in scCO₂-brine-sandstone systems. *Advances in Water Resources* 122, 278–290.
520 <https://doi.org/10.1016/j.advwatres.2018.10.020>
- 521 Gostick, J.T., Fowler, M.W., Ioannidis, M.A., Pritzker, M.D., Volkovich, Y.M., Sakars, A., 2006.
522 Capillary pressure and hydrophilic porosity in gas diffusion layers for polymer electrolyte fuel
523 cells. *Journal of Power Sources* 156, 375–387.
524 <https://doi.org/10.1016/j.jpowsour.2005.05.086>
- 525 Haines, W.B., 1930. Studies in the physical properties of soil. V. The hysteresis effect in capillary
526 properties, and the modes of moisture distribution associated therewith. *The Journal of*
527 *Agricultural Science* 20, 97–116.
- 528 Joekar-Niasar, V., Prodanović, M., Wildenschild, D., Hassanizadeh, S.M., 2010. Network model
529 investigation of interfacial area, capillary pressure and saturation relationships in granular
530 porous media: NEW NETWORK MODEL FOR CAPILLARY FLOW. *Water Resources Research* 46.
531 <https://doi.org/10.1029/2009WR008585>
- 532 Khishvand, M., Alizadeh, A.H., Oraki Kohshour, I., Piri, M., Prasad, R.S., 2017. In situ characterization
533 of wettability alteration and displacement mechanisms governing recovery enhancement
534 due to low-salinity waterflooding: PHYSICS OF LOW-SALINITY WATERFLOODING. *Water*
535 *Resources Research* 53, 4427–4443. <https://doi.org/10.1002/2016WR020191>
- 536 Khishvand, M., Alizadeh, A.H., Piri, M., 2016. In-situ characterization of wettability and pore-scale
537 displacements during two- and three-phase flow in natural porous media. *Advances in Water*
538 *Resources* 97, 279–298. <https://doi.org/10.1016/j.advwatres.2016.10.009>
- 539 Li, T., Schlüter, S., Dragila, M.I., Wildenschild, D., 2018. An improved method for estimating capillary
540 pressure from 3D microtomography images and its application to the study of disconnected
541 nonwetting phase. *Advances in Water Resources* 114, 249–260.
542 <https://doi.org/10.1016/j.advwatres.2018.02.012>
- 543 Lorensen, W.E., Cline, H.E., 1987. Marching cubes: A high resolution 3D surface construction
544 algorithm, in: *ACM Siggraph Computer Graphics*. ACM, pp. 163–169.

- 545 Ma, S., Mason, G., Morrow, N.R., 1996. Effect of contact angle on drainage and imbibition in regular
546 polygonal tubes. *Colloids and Surfaces A: Physicochemical and Engineering Aspects* 117, 273–
547 291. [https://doi.org/10.1016/0927-7757\(96\)03702-8](https://doi.org/10.1016/0927-7757(96)03702-8)
- 548 Mercer, J.W., Cohen, R.M., 1990. A review of immiscible fluids in the subsurface: Properties, models,
549 characterization and remediation. *Journal of Contaminant Hydrology* 6, 107–163.
550 [https://doi.org/10.1016/0169-7722\(90\)90043-G](https://doi.org/10.1016/0169-7722(90)90043-G)
- 551 Mokso, R., Schlepütz, C.M., Theidel, G., Billich, H., Schmid, E., Celcer, T., Mikuljan, G., Sala, L.,
552 Marone, F., Schlumpf, N., others, 2017. GigaFRoST: the gigabit fast readout system for
553 tomography. *Journal of synchrotron radiation* 24, 1250–1259.
- 554 Morrow, N.R., 1990. Wettability and Its Effect on Oil Recovery. *Journal of petroleum technology* 42,
555 1–476.
- 556 Morrow, N.R., 1970. Physics and Thermodynamics of Capillary Action in Porous Media. *Ind. Eng.*
557 *Chem.* 62, 32–56. <https://doi.org/10.1021/ie50726a006>
- 558 Murison, J., Semin, B., Baret, J.-C., Herminghaus, S., Schröter, M., Brinkmann, M., 2014. Wetting
559 Heterogeneities in Porous Media Control Flow Dissipation. *Physical Review Applied* 2.
560 <https://doi.org/10.1103/PhysRevApplied.2.034002>
- 561 Myers, G.R., Kingston, A.M., Varslot, T.K., Turner, M.L., Sheppard, A.P., 2011. Dynamic tomography
562 with a priori information. *Applied optics* 50, 3685–3690.
- 563 Quéré, D., 2008. Wetting and Roughness. *Annual Review of Materials Research* 38, 71–99.
564 <https://doi.org/10.1146/annurev.matsci.38.060407.132434>
- 565 Rabbani, H.S., Zhao, B., Juanes, R., Shokri, N., 2018. Pore geometry control of apparent wetting in
566 porous media. *Scientific Reports* 8. <https://doi.org/10.1038/s41598-018-34146-8>
- 567 Raeini, A.Q., Bijeljic, B., Blunt, M.J., 2018. Generalized network modeling of capillary-dominated two-
568 phase flow. *Physical Review E* 97. <https://doi.org/10.1103/PhysRevE.97.023308>
- 569 Reynolds, C.A., Krevor, S., 2015. Characterizing flow behavior for gas injection: Relative permeability
570 of CO₂-brine and N₂-water in heterogeneous rocks: CHARACTERIZING FLOW BEHAVIOR
571 FOR GAS INJECTION. *Water Resources Research* 51, 9464–9489.
572 <https://doi.org/10.1002/2015WR018046>
- 573 Scanziani, A., Singh, K., Blunt, M.J., Guadagnini, A., 2017. Automatic method for estimation of in situ
574 effective contact angle from X-ray micro tomography images of two-phase flow in porous
575 media. *Journal of Colloid and Interface Science* 496, 51–59.
576 <https://doi.org/10.1016/j.jcis.2017.02.005>
- 577 Schlüter, S., Berg, S., Li, T., Vogel, H.-J., Wildenschild, D., 2017. Time scales of relaxation dynamics
578 during transient conditions in two-phase flow: RELAXATION DYNAMICS. *Water Resources*
579 *Research* 53, 4709–4724. <https://doi.org/10.1002/2016WR019815>
- 580 Schlüter, S., Berg, S., Rücker, M., Armstrong, R.T., Vogel, H.-J., Hilfer, R., Wildenschild, D., 2016. Pore-
581 scale displacement mechanisms as a source of hysteresis for two-phase flow in porous
582 media. *Water Resources Research* 52, 2194–2205. <https://doi.org/10.1002/2015WR018254>
- 583 Schmatz, J., Urai, J.L., Berg, S., Ott, H., 2015. Nanoscale imaging of pore-scale fluid-fluid-solid contacts
584 in sandstone: Imaging Fluid-Fluid-Solid Contacts. *Geophysical Research Letters* 42, 2189–
585 2195. <https://doi.org/10.1002/2015GL063354>
- 586 Seth, S., Morrow, N.R., 2007. Efficiency of the Conversion of Work of Drainage to Surface Energy for
587 Sandstone and Carbonate. *SPE Reservoir Evaluation & Engineering* 10, 338–347.
588 <https://doi.org/10.2118/102490-PA>
- 589 Singh, K., Bijeljic, B., Blunt, M.J., 2016. Imaging of oil layers, curvature and contact angle in a mixed-
590 wet and a water-wet carbonate rock. *Water Resources Research* 52, 1716–1728.
591 <https://doi.org/10.1002/2015WR018072>
- 592 Singh, K., Jung, M., Brinkmann, M., Seemann, R., 2019. Capillary-Dominated Fluid Displacement in
593 Porous Media. *Annual Review of Fluid Mechanics* 51, 429–449.
594 <https://doi.org/10.1146/annurev-fluid-010518-040342>

- 595 Singh, K., Menke, H., Andrew, M., Lin, Q., Rau, C., Blunt, M.J., Bijeljic, B., 2017. Dynamics of snap-off
596 and pore-filling events during two-phase fluid flow in permeable media. *Scientific Reports* 7.
597 <https://doi.org/10.1038/s41598-017-05204-4>
- 598 Singh, K., Menke, H., Andrew, M., Rau, C., Bijeljic, B., Blunt, M.J., 2018. Time-resolved synchrotron X-
599 ray micro-tomography datasets of drainage and imbibition in carbonate rocks. *Scientific Data*
600 5. <https://doi.org/10.1038/sdata.2018.265>
- 601 Spurin, C., Krevor, S.C., Blunt, M.J., Berg, S., Bijeljic, B., Bultreys, T., Rücker, M., Garfi, G., Scanziani, A.,
602 Schlepütz, C.M., others, 2019. Imaging of Steady-State Intermittent Flow Pathways in a
603 Carbonate Rock with 1 Second Time Resolution, in: AGU Fall Meeting 2019. AGU.
- 604 Sun, C., McClure, J.E., Mostaghimi, P., Herring, A.L., Shabaninejad, M., Berg, S., Armstrong, R.T., 2020.
605 Linking continuum-scale state of wetting to pore-scale contact angles in porous media.
606 *Journal of Colloid and Interface Science* 561, 173–180.
607 <https://doi.org/10.1016/j.jcis.2019.11.105>
- 608 Verma, R., Icardi, M., Prodanović, M., 2018. Effect of wettability on two-phase quasi-static
609 displacement: Validation of two pore scale modeling approaches. *Journal of Contaminant*
610 *Hydrology* 212, 115–133. <https://doi.org/10.1016/j.jconhyd.2018.01.002>
- 611 Wenzel, R.N., 1936. RESISTANCE OF SOLID SURFACES TO WETTING BY WATER. *Industrial &*
612 *Engineering Chemistry* 28, 988–994. <https://doi.org/10.1021/ie50320a024>
- 613 Wildenschild, D., Sheppard, A.P., 2013. X-ray imaging and analysis techniques for quantifying pore-
614 scale structure and processes in subsurface porous medium systems. *Advances in Water*
615 *Resources* 51, 217–246. <https://doi.org/10.1016/j.advwatres.2012.07.018>
- 616 Zhao, B., MacMinn, C.W., Primkulov, B.K., Chen, Y., Valocchi, A.J., Zhao, J., Kang, Q., Bruning, K.,
617 McClure, J.E., Miller, C.T., Fakhari, A., Bolster, D., Hiller, T., Brinkmann, M., Cueto-Felgueroso,
618 L., Cogswell, D.A., Verma, R., Prodanović, M., Maes, J., Geiger, S., Vassvik, M., Hansen, A.,
619 Segre, E., Holtzman, R., Yang, Z., Yuan, C., Chareyre, B., Juanes, R., 2019. Comprehensive
620 comparison of pore-scale models for multiphase flow in porous media. *Proceedings of the*
621 *National Academy of Sciences* 116, 13799–13806. <https://doi.org/10.1073/pnas.1901619116>
622